Harmonic to subharmonic transition of the Faraday instability in miscible fluids

Antoine Briard,[1,*] Benoît-Joseph Gréa,[2] and Louis Gostiaux[3]
[1]*Centre de Mathématiques et de Leurs Applications, CNRS, ENS Paris-Saclay, Université Paris-Saclay, 94235, Cachan Cedex, France*
[2]*DIF, DAM, CEA, Arpajon, France*
[3]*LMFA UMR 5509 CNRS, Université de Lyon, École Centrale 69130 Écully Lyon, France*

(Received 1 August 2018; published 19 April 2019)

When a stable stratification between two miscible fluids is excited by a vertical and periodic forcing, a turbulent mixing zone can develop, triggered by the Faraday instability. The mixing zone grows and saturates to a recently predicted final value L_{sat} [Gréa and Ebo Adou, J. Fluid Mech. **837**, 293 (2018)] when resonance conditions are no longer fulfilled. Notably, it is expected from the Mathieu stability diagram that the instability may evolve from a harmonic to a subharmonic regime for particular initial conditions. This transition is evidenced here in the full inhomogeneous system using direct numerical simulations with 1024^3 points: the analysis of one-point statistics and spectra reveals that turbulence is greatly enhanced after the transition, while the global anisotropy of both the velocity and concentration fields is significantly reduced. Furthermore, using the concept of sorted density field, we compute the background potential energy e_p^b of the flow, which increases only after the transition as a signature of irreversible mixing. While the gain in e_p^b strongly depends on the control parameters of the instability, the cumulative mixing efficiency is more robust. At saturation of the instability, available potential energy is partially released in the flow as background potential energy. Finally, it is shown numerically that for fixed parameters, a multiple-frequency forcing can modify the duration of the harmonic regime without significantly altering the asymptotic state.

DOI: 10.1103/PhysRevFluids.4.044502

I. INTRODUCTION

When a two-layer system of immiscible fluids is vertically excited by a periodic forcing term, the interface can be destabilized as a result of the Faraday instability [1]. This parametric instability is well known for producing a great variety of structures at the interface, whose pattern formation has been widely investigated [2,3].

For miscible fluids as considered here, a turbulent mixing zone $L(t)$ may appear and grow in size [4,5]: turbulent kinetic and potential energies are produced by the periodic forcing as long as internal gravity waves keep being excited by the parametric resonances [6]. However, this mechanism cannot be sustained since the mean density gradient decreases when $L(t)$ increases. This leads to a final state characterized by an asymptotic mixing layer of width L_{end}. Most of the research on this topic, numerical and experimental, focused on the onset of the instability more than its asymptotic state, until recently: indeed, in Ref. [7], the authors derived analytically a prediction for the asymptotic

*antoine.briard@hotmail.fr

size of the mixing zone when the instability saturates,

$$L_{\text{sat}} = \frac{2\mathcal{A}_t G_0}{\omega^2}(2F + 4), \tag{1}$$

where G_0 is the gravitational acceleration, F the acceleration ratio or forcing intensity, ω the forcing pulsation, and $\mathcal{A}_t = \frac{\rho_1 - \rho_2}{\rho_1 + \rho_2}$ the Atwood number for the heavy and light fluids of density ρ_1 and ρ_2, respectively. In Ref. [7] the final sizes of the mixing zone L_{end} obtained numerically were successfully compared to the prediction L_{sat} for a wide range of parameters and initial conditions. The assumptions made to derive (1) are not recalled here for the sake of brevity and can be found in Ref. [7].

In Ref. [7] it was notably recovered that the instability is dominantly subharmonic as in Refs. [3,4,6,8]: more precisely from the experimental point of view, the various perturbations in concentration c and velocity $\mathbf{u}$ oscillate at frequency $\omega/2$, half as fast as the vessel containing the two fluids. Meanwhile, it can be shown that the mixing zone $L(t)$ oscillates at frequency ω in the subharmonic regime.

An additional outcome of Ref. [7] was the observation, for some particular initial conditions, of a harmonic to subharmonic transition of the instability, namely, at short time, the concentration and velocity fluctuations oscillate at frequency ω as fast as the forcing. This is quite intricate to observe since the harmonic regime is rather short: indeed, as soon as the mixing zone size $L(t)$ grows slightly from its initial value, the instability rapidly becomes subharmonic, as illustrated later. However, this transition was observed only with direct numerical simulations (DNSs) within a homogeneous framework. In such a case, the computational domain is centered in the mixing zone where the mean concentration gradient is linear. The transition was not observed with DNSs of the full inhomogeneous system.

Therefore, the challenge of the present work is to observe the harmonic to subharmonic transition of the Faraday instability between two miscible fluids in the full inhomogeneous system, using high-resolution DNSs. The underlying objective is to characterize this transition in terms of global anisotropy and turbulent features using one-point statistics and scale-by-scale information. Notably, it will be shown numerically that the global anisotropy and turbulent intensity significantly differ between the harmonic and subharmonic regimes, and that the transition of the instability triggers the turbulence from the initial (almost) laminar slightly perturbed state.

An additional challenge is to determine the amount of irreversible mixing induced at small scales by the turbulent stirring. To do so, the concepts of sorted concentration fields and background potential energy are used [9]: this notably permits us to link the increase of background potential energy Δe_p^b to the saturated mixing zone size L_{sat} and to further compute the cumulative mixing efficiency η_b^c of the flow [10].

Finally, using a multiple-frequency forcing, we propose a way to shorten the duration of the harmonic regime when a constraint on the forcing intensity F is imposed: the multiple-frequency is chosen such that the final state prediction (1) is not altered.

Hence, the main new features addressed in the present work are threefold:

(1) The transition from the harmonic to subharmonic regime in the full inhomogeneous system is evidenced here. In Ref. [7] it was observed only within a homogeneous framework, and there was no guarantee it would be the case starting from an interface. This transition is then characterized using one-point turbulent statistics.

(2) With the background potential energy, we quantify the irreversible mixing of this turbulent instability. In particular, we explain why in Ref. [7] the final size of the mixing zone obtained numerically L_{end} slightly exceeds the prediction L_{sat}. Among three definitions for the mixing efficiency, we exhibit a robust one and show some dependence on the control parameters.

(3) We show how a multiple-frequency forcing can impact the harmonic regime.

The paper is organized as follows: the main equations and stability analysis are given in Sec. II, along with some details about the DNSs. All the results regarding the transition are gathered in Sec. III. More precisely, we first investigate the time evolution of the mixing zone; then one-point

statistics and global anisotropy are used to characterize the turbulent structures dynamics. Moreover, a scale-by-scale analysis of turbulent spectra is proposed as well. Afterwards, the background potential energy is analyzed in Sec. IV to quantify the irreversible mixing produced by the flow and to evaluate the associated mixing efficiency. In Sec. V effects of a multiple-frequency forcing on the harmonic regime duration are briefly discussed. Conclusions are gathered in the last section.

II. PREDICTION, STABILITY, AND NUMERICAL DETAILS

In this section, the equations for the velocity and concentration fields are given, along with the main steps yielding the prediction for the saturated mixing zone size (1), and then some technical details about the DNSs are provided.

A. The saturated mixing zone size

The starting point is the equations for the total velocity $\boldsymbol{U}$ and concentration C fields under vertical periodic forcing within the Boussinesq approximation:

$$\frac{\partial \boldsymbol{U}}{\partial t} + (\boldsymbol{U}\cdot\boldsymbol{\nabla})\boldsymbol{U} = -\boldsymbol{\nabla}P - 2\mathcal{A}_t G_0\,\boldsymbol{n_3}[1+F\cos(\omega t)]C + \nu\nabla^2\boldsymbol{U}, \tag{2}$$

$$\frac{\partial C}{\partial t} + (\boldsymbol{U}\cdot\boldsymbol{\nabla})C = \kappa\nabla^2 C, \tag{3}$$

where ν and κ are the kinematic viscosity and scalar diffusivity, respectively, and P the reduced pressure. The heavy fluid is such that $C(\rho_1)=1$ and the light one such that $C(\rho_2)=0$, with for the density fluctuation ρ',

$$\frac{\rho'}{\rho_0} = 2\mathcal{A}_t\left(C-\frac{1}{2}\right), \tag{4}$$

where $\rho_0=(\rho_1+\rho_2)/2$ is the reference density. The concentration field being inhomogeneous in the vertical direction $\boldsymbol{n_3}$, it is convenient to define a spatial average for the two horizontal directions $\langle\cdot\rangle_H$. Hence, one has $C=c+\langle C\rangle_H$, where the fluctuating part verifies $\langle c\rangle_H=0$. Of particular interest, the equation for the fluctuating concentration field becomes

$$\frac{\partial c}{\partial t} + u_j\frac{\partial c}{\partial x_j} = -u_3\frac{\partial\langle C\rangle_H}{\partial x_3} + \frac{\partial\langle u_3 c\rangle_H}{\partial x_3} + \kappa\nabla^2 c. \tag{5}$$

Within the homogeneous framework [11], the mean concentration profile can be approximated by $\partial_3\langle C\rangle_H=-1/L$, where the mixing zone size is defined as

$$L(t) = 6\int\langle C\rangle_H(z,t)[1-\langle C\rangle_H(z,t)]\,dz. \tag{6}$$

After some algebra detailed in Refs. [7,11], where viscous effects and fluctuation-fluctuation nonlinearities are discarded, one eventually obtains the following equation:

$$\frac{\partial^2\mathcal{C}}{\partial t^2} + \frac{\dot{L}}{L}\frac{\partial\mathcal{C}}{\partial t} + N^2(t)\sin^2(\theta)[1+F\cos(\omega t)]\mathcal{C}(t,\theta)=0, \tag{7}$$

where $N^2=2\mathcal{A}_t G_0/L$ is the stratification (or Brunt-Väisälä) frequency, and θ is the angle formed by the vertical axis $\boldsymbol{n_3}$ and the wave vector $\boldsymbol{k}$. The convenient variable $\mathcal{C}$ is the square root of the $k=|\boldsymbol{k}|$-integrated concentration variance spectrum: hence, the concentration variance can be expressed as $\langle c^2\rangle=\int_0^\pi \mathcal{C}^2(t,\theta)\sin(\theta)\,d\theta$, where $\langle\cdot\rangle$ is the volume average. For a given mixing zone size $L(t)$, one can investigate the fluctuations around this turbulent state, which yields an infinite set of decoupled Mathieu oscillators

$$\frac{\partial^2\mathcal{C}}{\partial t^2} + N^2\sin^2\theta[1+F\cos(\omega t)]\mathcal{C}=0. \tag{8}$$

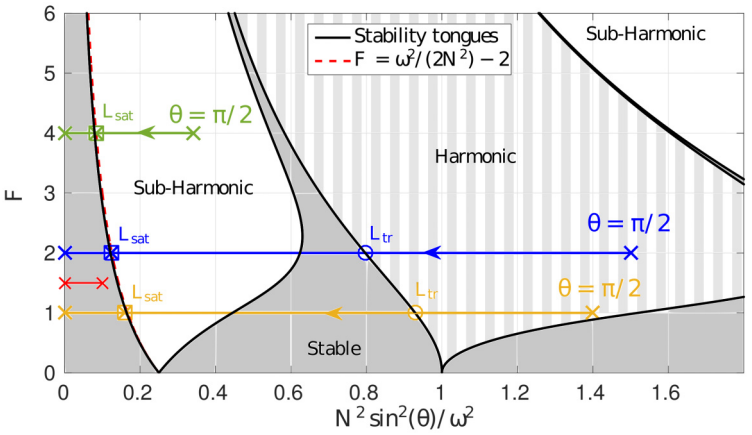

FIG. 1. Mathieu diagram: stability curves (black) separate stable regions (gray) from harmonic and subharmonic unstable regions. The marginal stability curve is displayed as a dashed red curve. The various initial conditions, delimited by crosses (×; from $\theta = 0$ to $\theta = \pi/2$), are discussed in the text.

The stability diagram of this equation can be obtained by performing a classical Floquet analysis [12–14] by expanding $\mathcal{C} = \sum_n y_n e^{i(\alpha+n\omega)t}$, where $\alpha = 0$ and $\alpha = \omega/2$ are for the harmonic and subharmonic stability curves, respectively. This yields the stability diagram of Fig. 1, with the forcing parameter F as a function of the eigenvalues $(N \sin\theta/\omega)^2$. The details on how to read and understand the stability diagram are given below.

For a given initial condition at a fixed F, a whole horizontal segment delimited by two crosses is excited: the left-hand side extremity corresponds to $\theta = 0$, and the right-hand side (rhs) to $\theta = \pi/2$. Hence, at each time t, the extent of the segment is $[0; (N/\omega)^2]$, where the rhs extremity $(N/\omega)^2$ corresponds to the mixing zone size L. Two cases should be distinguished:

(1) The instability is not triggered, and the mixing zone size remains at its initial value $L(t = 0) = L_0$. This corresponds to the initial segment being entirely in the gray stable region at left, such as the one delimited by the two red crosses in Fig. 1.

(2) The instability is triggered when the rhs extremity $(N/\omega)^2$ of the excited segment falls beyond the marginal stability curve. Some θ-modes are excited, and hence $L(t)$ grows in size. Thus, $(N/\omega)^2$ decreases and goes toward the left of the diagram, indicated by arrows.

There are two unstable configurations:

(1) The initial condition is in the first subharmonic region (green cross). Hence $L(t)$ grows as a result of the instability, and thus the rhs extremity of the initial excited segment evolves up to the marginal stability curve given by $2F + 4 = \omega^2/N^2$. The saturated state $L_{\rm sat}$, whose prediction (1) was first given in Ref. [7], is indicated by a square.

(2) The initial condition is in the harmonic region (yellow and blue crosses) or beyond. Both harmonic and subharmonic θ-modes are excited. In the cases pictured in Fig. 1, the most unstable modes ($\theta \simeq \pi/2$) are in the first harmonic tongue, so that the harmonic regime will be more observable. At some point during the growth of $L(t)$, the rhs extremity of the segment $[0; N^2/\omega^2]$ will cross the gray stable zone, indicated by a circle in Fig. 1. This corresponds to a size L_{tr} where no more θ-modes are in the harmonic region: this is precisely the phenomenon we wish to observe numerically.

From now on, we define the *harmonic to subharmonic transition* as the size L_{tr} of the mixing zone (and corresponding time) from which no more harmonic modes are excited. Two regimes for the transition are illustrated in Fig. 1, namely, at small ($F = 1$) and larger ($F = 2$) forcing parameters. One may think that the $F = 2$ configuration permits us to better observe the transition since the harmonic tongue is larger. This is misleading, since in fact for a stronger F, the mixing zone evolves

sharply at short times [see Fig. 3(a) below], so that the harmonic regime can hardly be seen. Hence, the harmonic regime can be well observed for moderate F (like $F = 1$), but not too small as well, otherwise most of the excited modes are either in stable regions or damped by viscous effects [13]. Before moving on with the numerical setup, we come back to the assumptions yielding (8). It will be shown in what follows that the saturation criterion (1) is well verified by the DNSs, in agreement with Ref. [7]. The reasons why this criterion works well are twofold. First, the model equation (8) implicitly takes into account some effects of turbulence through the time evolution of $N(t)$: hence, even though nonlinear transfers are neglected, the nonlinear interaction between fluctuations and the mean field is kept. Second, large scales are mainly driven by linear production of energy: this is well illustrated by small values of the Froude number in Fig. 6(a) below. This shows that turbulence is weak compared to the buoyancy production and therefore cannot decisively change the stability of the flow particularly close to the saturation.

B. Numerical setup

We perform direct numerical simulations (DNSs) of the Navier-Stokes-Boussinesq equations (2) and (3) on a triply periodic cubic box of size $2\pi \times 2\pi \times 2\pi$. A classical spectral Fourier collocation method is used with two-third rule dealiasing. The code is parallelized using Message Passing Interface (MPI) and slab-shaped domain decomposition, so that the present simulations with 1024^3 points are performed using 1024 cores. The time increment is determined using a third-order low-storage strong-stability-preserving Runge-Kutta scheme, with implicit treatment of viscous terms.

In the present numerical work, which uses a pseudospectral code, one has to ensure periodicity in the vertical inhomogeneous direction: this was not an issue in the DNSs of Ref. [7], performed either in physical space or within a homogeneous framework. To overcome this difficulty, we choose an initial condition in which the scalar field changes sharply from its light to heavy value at the vertical boundaries:

$$C(\boldsymbol{x}, t = 0) = \frac{1}{2}\left[1 + \tanh\left(\frac{z - \pi}{\sigma}\right)\right] + C_{\text{inh}}(\boldsymbol{x}),$$
$$C_{\text{inh}}(\boldsymbol{x}) = -\frac{1}{2}\left\{\tanh\left(\frac{z}{0.01}\right) + \tanh\left[\frac{z - (2\pi - 2\pi/N)}{0.01}\right]\right\}. \tag{9}$$

The first term is the true concentration profile, in which the parameter σ is used to modify the initial mixing zone size $L_0 = L(t = 0)$. In the present simulations, we set $\sigma = 0.01$, so that $L_0 \simeq 0.07$ for $\mathcal{A}_t = 0.01$ and $L_0 \simeq 0.04$ for $\mathcal{A}_t = 0.02$. The remaining term C_{inh} ensures vertical periodicity at the boundaries. Perturbations of intensity $\langle c^2\rangle(t = 0)/5$, smoothed by a Gaussian filter, are added to this initial concentration profile (9).

However, without a particular treatment at the vertical boundaries, a Rayleigh-Taylor instability can be triggered in the two unstable regions introduced at the top and bottom of our domain to ensure periodicity. To avoid this undesirable phenomenon, a penalization method is implemented, inspired from Ref. [15]. In other words, two penalized bands are added at the top and bottom of the box, namely, for $z \in [0; L_\eta/2]$ and $z \in [2\pi - L_\eta/2; 2\pi]$, where $L_\eta/2$ is the height of each penalized band. Basically, a new term is added in the rhs of (2) to mimic a porous media, $\partial_t \boldsymbol{u} + (\boldsymbol{u} \cdot \boldsymbol{\nabla})\boldsymbol{u} = \cdots - \chi \boldsymbol{u}/\eta$, where η is the penalization parameter, and χ the mask function. The penalization parameter is set either to $\eta = 5 \times 10^{-3}$ or $\eta = 10^{-2}$ for an explicit time-integration scheme, with no noticeable differences. The penalization mask χ is here a simple door function $D(\boldsymbol{x})$, equal to 1 in the "solid" domain and 0 in the fluid one. To avoid Gibbs oscillations, the mask is further filtered in spectral space using

$$D(\boldsymbol{x}) = \begin{cases} 0 & \text{for} \quad L_\eta/2 \leqslant z \leqslant 2\pi - L_\eta/2, \\ 1 & \text{for} \quad z \text{ otherwise}, \end{cases}, \quad \chi(\boldsymbol{k}) = \hat{D}(\boldsymbol{k}) \exp\left(-C_\eta \frac{k^2}{N^2}\right), \tag{10}$$

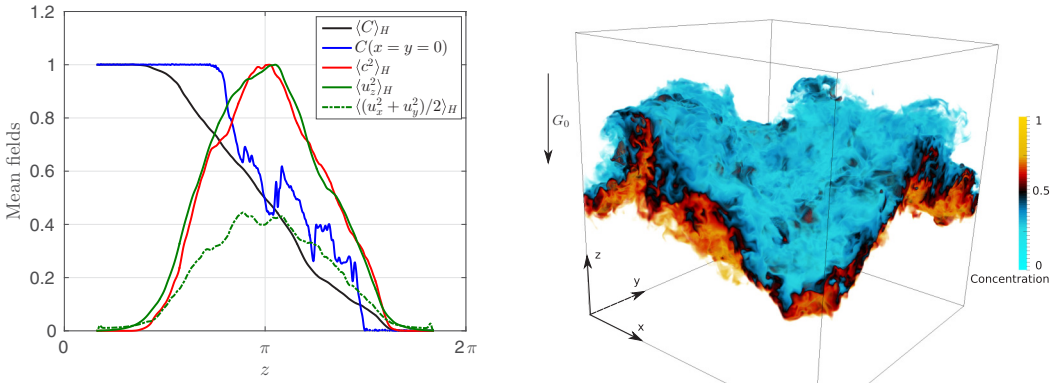

FIG. 2. Run F1A01 at $\omega t = 76$. (a) Vertical profiles in the nonpenalized domain: horizontal average of the concentration $\langle C\rangle_H$, variance $\langle c^2\rangle_H$, and energies $\langle u_i^2\rangle_H$ (normalized by $\max\langle u_z^2\rangle_H$), with total concentration $C(x = y = 0, z)$. (b) Snapshot of the 3D concentration field.

where $\hat{}$ denotes the Fourier transform. N is the number of points in one direction, and we choose $C_\eta = 256$, which preserves both the shape and intensity of the mask. Multiplying or dividing the value of C_η by a factor 2 does not modify the results with our spatial resolution. If we call d_{inh} the length where the vertical periodicity is ensured by C_{inh}, it is fully covered by the penalized bands with $L_\eta > 2d_{\text{inh}}$, which guarantees the reliability of the results. Obviously, in what follows, these penalized bands were excluded when computing averaged quantities.

In conclusion, the penalization method ensures periodicity in the vertical inhomogeneous direction and fully prevents the triggering of the Rayleigh-Taylor instability. Multiple DNSs (not presented) were conducted with both 512^3 and 1024^3 points to verify that the mask holds on even for large forcing parameters ($4 \leqslant F \leqslant 8$). An example is provided in Fig. 2(a) for run F1A01, defined hereafter in Table I. The strong oscillations of the concentration field are well smoothed by the horizontal averaging, resulting in the almost linear mean concentration profile between the

TABLE I. Parameters of the DNSs with 1024^3 points, ordered by increasing F. Forcing intensity F; Atwood number $\mathcal{A}_t$; pulsation ω; Integral wave number of the concentration field k_{peak}; kinematic viscosity $\nu = \kappa$; gravitational acceleration G_0; initial size of the mixing zone $L(t = 0) = L_0$; predicted saturated size L_{sat}; gain in background potential energy Δe_p^b and final cumulative mixing efficiency η_b^c, both defined in Sec. IV; multiple-frequency parameter b, defined in Sec. V.

Run name	F	$\mathcal{A}_t$	ω	k_{peak}	ν	G_0	L_0	L_{sat}	Δe_p^b	η_b^c	b
F055A015	0.55	0.015	3.46	20	1×10^{-4}	65	0.06	0.83	0.058	0.420	0
F07A045	0.7	0.045	4.29	20	1×10^{-4}	65	0.04	1.72	0.958	0.410	0
F1A01	1.0	0.01	0.7	30	1×10^{-4}	10	0.07	2.45	0.079	0.415	0
F1A01b05	1.0	0.01	0.7	30	1×10^{-4}	10	0.07	2.45	0.064	0.421	0.5
F1A01b1	1.0	0.01	0.7	30	1×10^{-4}	10	0.07	2.45	0.063	0.415	1
F1A02	1.0	0.02	1.0	30	1×10^{-4}	10	0.04	2.40	0.154	0.420	0
F1A02L0	1.0	0.02	1.0	30	1×10^{-4}	10	0.30	2.40	0.154	0.420	0
F1A02k5	1.0	0.02	1.0	5	1×10^{-4}	10	0.04	2.40	0.154	0.420	0
F1A1	1.0	0.1	2.2	30	2×10^{-4}	10	0.03	2.48	0.734	0.413	0
F2A01	2.0	0.01	0.8	30	1×10^{-4}	10	0.07	2.50	0.081	0.391	0
F5A01	5.5	0.01	1.0	30	1×10^{-4}	10	0.31	3.00	0.114	0.254	0
F8A02	8.0	0.02	2.0	30	1×10^{-4}	10	0.05	2.00	0.111	0.198	0

regions where $C = 0$ and $C = 1$ for the light and heavy fluids, respectively. The three-dimensional (3D) concentration field at the same time is presented in Fig. 2(b).

Finally, the parameters of the different DNSs presented in this work are summarized in Table I. The kinetic energy is initially zero and is thus fully created by the instability. The Schmidt number is unit, meaning $\nu = \kappa$. The wave number k_{peak} corresponds to the maximum of the initial concentration variance spectrum.

The idea behind the choice of parameters in Table I is the following one: the runs with $1 \leqslant F \leqslant 2$ and $b = 0$ yield similar asymptotic states L_{sat}, but with different transients, and are analyzed in Sec. III. The two runs with $b \neq 0$ are compared with run F1A01 in Sec. V for the multiple-frequency case. The runs with either $F < 1$ or $F > 2$ are briefly presented in Appendix. The impact of changing the initial conditions such as L_0 and k_{peak} is investigated with runs F1A02, F1A02k5, and F1A02L0. The gain in background potential energy Δe_p^b and final cumulative mixing efficiency η_b^c are defined and discussed later in Sec. IV.

III. THE HARMONIC TO SUBHARMONIC TRANSITION

In this section, the results regarding the harmonic to subharmonic transition of the Faraday instability are given. First, the time evolution of the mixing zone is addressed, with various transients yielding similar asymptotic states. Then, the emphasis is put on one-point statistics and the global anisotropy of the velocity and concentration fields to characterize turbulent structures. Finally, a scale-by-scale study of turbulent spectra is proposed.

A. Mixing zone size

In this section we are interested in the time evolution of the mixing zone size $L(t)$, defined in Eq. (6), on the triggering of the instability and on the asymptotic states. Four runs are presented in Fig. 3(a): for some of them, 3D videos of the scalar field made with Paraview are proposed. These configurations have almost the same prediction L_{sat} (see Table I), and hence comparable final size L_{end} in the asymptotic state, but different transients.

The transition size L_{tr}, defined in Sec. II, corresponds to the size from which harmonic modes are no longer excited, as shown in Fig. 1. The values of L_{tr} are quite similar for the runs presented in Fig. 3(a): $L_{tr} \simeq 0.44$, reported as $-\cdot$ horizontal lines. Since all modes $\theta \in [0; \pi/2]$ are excited at each time, this value of L_{tr} can be crossed several times, like for $F = 1$, or only once, like for $F = 2$. The last time for which L_{tr} is crossed corresponds to the transition from the harmonic to subharmonic regime and is indicated by a vertical dashed line: for instance, this is at $\omega t = 44$ for run F1A01.

As anticipated, the transition occurs much more rapidly for $F = 2$ than for $F = 1$; see videos for runs 1 and 2 in the Supplemental Material [16]. On the contrary, at $F = 1$, the transition is delayed with an increasing Atwood number in Fig. 3(a); see videos for runs 1 and 3 [16] for $\mathcal{A}_t = 0.1$. This is expected since it is requires more energy to mix fluids with a greater density contrast. Additional time evolutions of $L(t)$ are discussed in the Appendix for larger and smaller F.

In each case, the mixing zone size increases with intense oscillations only from the transition and during the subharmonic regime, where vertical structures develop, consistently with the vertical energy being greater than the horizontal one in Fig. 2(a). The mixing zone size $L(t)$ eventually saturates to a state which is larger than the prediction (1) by roughly 15%. This feature was already noticed in Ref. [7] and attributed to the simplicity of the model used to derive the saturation criterion. An important theoretical contribution of the present work is an explanation for this apparent discrepancy, which is provided in Sec. IV.

For illustration purposes, the concentration field of run F1A01 is presented in Fig. 3(b) at four different moments: close to the initial condition, in the harmonic regime where the oscillations are still quite small, after the transition within the subharmonic regime where the turbulent mixing zone

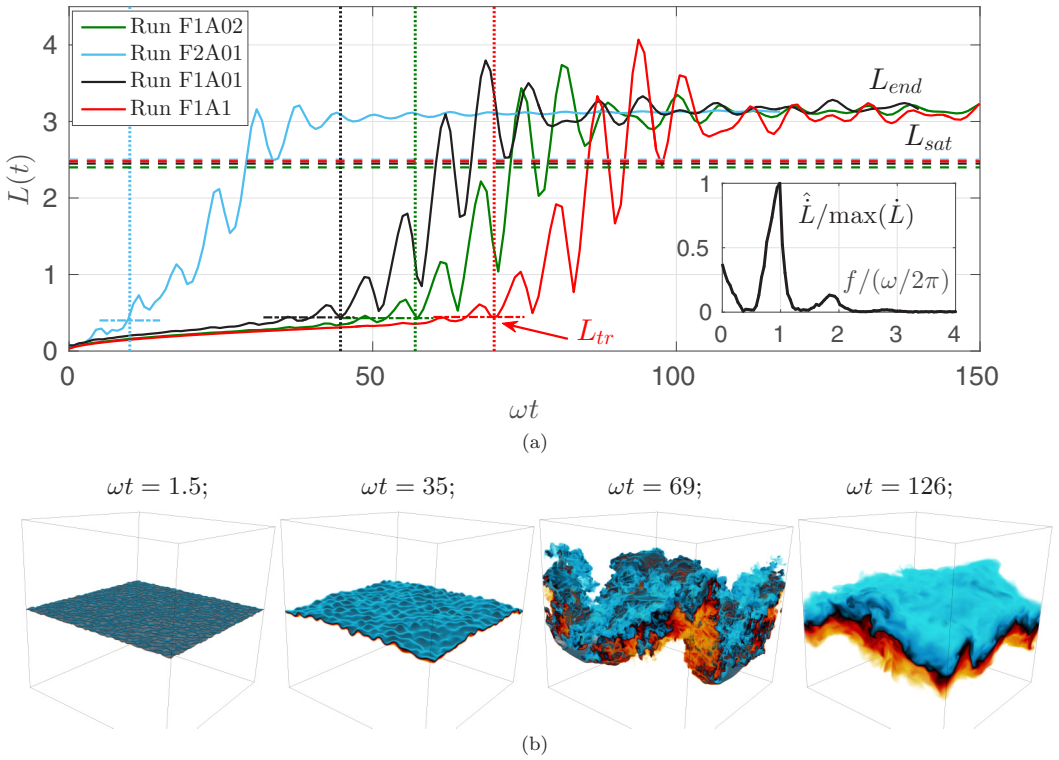

FIG. 3. (a) Mixing zone size $L(t)$ for runs F1A01 (black), F1A02 (dark green), F1A1 (red), and F2A01 (light blue); horizontal dashed lines correspond to the prediction (1). Vertical dashed lines indicate the separation between the harmonic and subharmonic regimes. Inset: Fourier transform of $\dot{L}$ as function of the normalized frequency for run F1A01. (b) Snapshot of the 3D concentration field of run F1A01 at four different times: colorbar same as Fig. 2(b).

size grows violently, and finally in the asymptotic state where the oscillations are smoother because of the weaker turbulence due to the instability saturation.

In the 3D videos of runs 1 and 3 with $F = 1$ [16], the transition is quite visible: the oscillation period of the small initial deformation is twice as fast as the later large amplitude beatings. However, from Fig. 3(a), the transition is hardly visible on $L(t)$. The Fourier transform of $\dot{L}$ is presented in the inset as function of the normalized frequency $2\pi f/\omega$. The first and most intense peak at $f = \omega/(2\pi)$ corresponds to the subharmonic regime. The second peak at $f = \omega/\pi$ corresponds to the harmonic regime. This is an observation of the harmonic to subharmonic transition: a more convincing proof is proposed in the next section.

Finally, we analyze in Fig. 4 the effects of changing the initial conditions k_{peak} and L_0 for a given set of control parameters $\mathcal{A}_t$, F and ω. The configuration of run F1A02 is used as a reference; in run F1A02L0, the initial mixing zone size is increased with the same k_{peak}, and on the contrary, k_{peak} is decreased in run F1A02k5 with the same L_0. The outcomes of Fig. 4 are threefold.

First, the asymptotic state L_{end} does not depend on k_{peak} or L_0, but only on the control parameters $\mathcal{A}_t$, F, and ω: this feature has been verified for other configurations in DNSs at lower resolution, not presented here for the sake of brevity. Second, increasing L_0 does not trigger the instability earlier, but decreasing k_{keap} does: indeed, the initial perturbation is less damped by viscous effects and is thus directly injected into the modes that will be amplified by the parametric instability: see videos of runs 1 and 4 [16] to observe the effects of the initial perturbation size. Third, the harmonic to subharmonic transition can be observed directly on $L(t)$ for run F1A02L0, with a clear

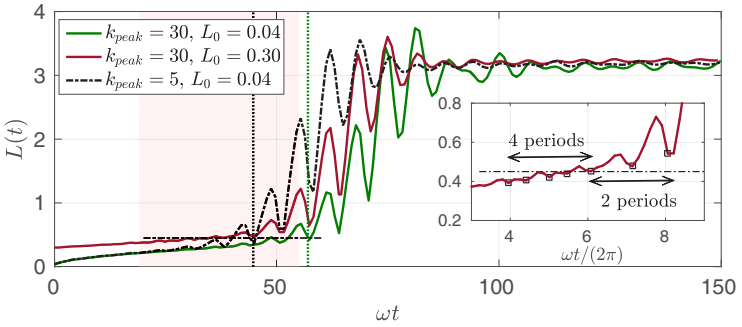

FIG. 4. Effects of initial conditions for the configuration of run F1A02 (green) reported here as a reference. Larger L_0 for run F1A02L0 (red) and smaller k_{peak} for run F1A02k5 (dashed black): horizontal and vertical lines as in Fig. 3(a). The shaded region corresponds to the inset, where $L(t)$ is plotted for run F1A02L0 as function of $\omega t/(2\pi)$: square symbols delimit the periods.

change of period in the inset of Fig. 4, unlike for runs F1A02 and F1A02k5. The reason is that for run F1A02L0, $N_0^2/\omega^2 = 1.33$ falls directly into the first harmonic tongue, whereas for F1A02 and F1A02k5, $N_0^2/\omega^2 = 10$, meaning that additional subharmonic tongues are excited and probably hide the harmonic resonance.

In conclusion, we have observed in the full inhomogeneous system that distinct sets of control parameters $[F, \omega, \mathcal{A}_t]$ may yield similar asymptotic states L_{end} with different transient regimes: in particular, a larger F shortens the harmonic regime, whereas a larger $\mathcal{A}_t$ lengthens it. For a given set $[F, \omega, \mathcal{A}_t]$, the initial conditions k_{peak} and L_0 only alter the transient, not the asymptotic state.

B. Structures and global anisotropy

Are the structures different in the two unstable regimes? To answer this question, we analyze the global anisotropy of the flow. The vertical anisotropy of the velocity field is defined as $\langle b_{33}\rangle_H(z) = \langle u_z^2\rangle_H/q^2 - 1/3$, where $q^2 = \langle u_i u_i\rangle_H$. The usual volume average b_{33} is obtained by integrating $\langle b_{33}\rangle_H$ along z (excluding the penalized bands). Remark that because of the initial condition with zero kinetic energy, b_{33} is not defined at $t = 0$.

The vertical anisotropy indicator b_{33} is presented in Fig. 5(a) for runs F1A01 and F1A1 with $F = 1$. The transition of the instability from a harmonic to a subharmonic regime can be seen since in the subharmonic part, the period is twice the one of the harmonic regime. This is better evidenced in Fig. 5(b), where we have zoomed in for run F1A1, as a function of $\omega t/(2\pi)$. In the harmonic regime, there are eight periods against four in the subharmonic one.

In the harmonic regime ($\omega t \leqslant 44$ for run F1A01, and $\omega t \leqslant 70$ for run F1A1), b_{33} is strongly different from the isotropic state $b_{33} = 0$, meaning that the velocity field is highly anisotropic and vertically elongated, consistently with gravity waves having an orientation close to $\theta = \pi/2$. Gravity waves with a smaller θ are excited as well in the first subharmonic tongue (see stability diagram in Fig. 1), which explains why two successive peaks of b_{33} do not have the same amplitude in the harmonic regime.

At the onset of the transition, the turbulence becomes stronger and global anisotropy decreases. Turbulent structures are also more inclined toward the horizontal plane, thus reducing the vertical anisotropy b_{33}: indeed, the modes with $\theta \simeq \pi/2$ become temporarily stable between the harmonic and subharmonic tongues, meaning that smaller angles dominate. Finally, when the gravity waves have again an angle of $\theta = \pi/2$ in the subharmonic regime, there is somehow a balance between structures being once again vertically elongated, and an enhanced return to isotropy due to a strengthening of turbulence.

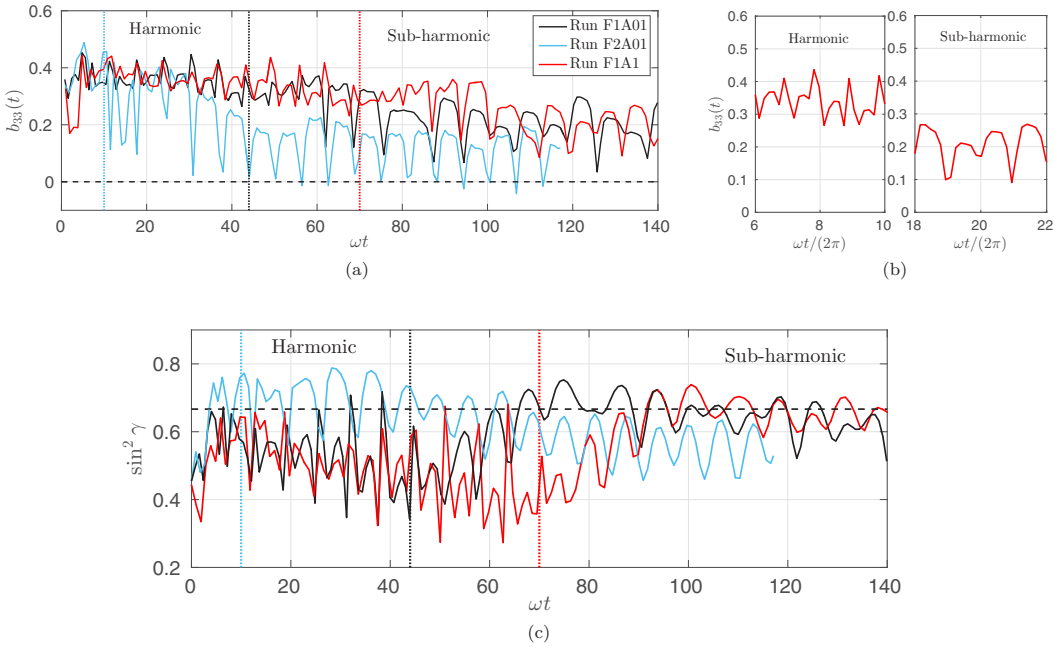

FIG. 5. Global anisotropy for runs F1A01 (black), F1A1 (red), and F2A01 (light blue); vertical dashed lines indicate the separation between the harmonic and subharmonic regimes. (a) Vertical anisotropy of the velocity field b_{33}. (b) Zoom for run F1A1 as a function of $\omega t/(2\pi)$. (c) Concentration field anisotropy $\sin^2\gamma$.

For run F2A01 with $F = 2$, because of the stronger forcing intensity, the transition happens more rapidly so that the vertical anisotropy decays faster. In the asymptotic state, the vertical anisotropy for $F = 2$ is smaller than for $F = 1$, very likely because for $F = 2$ the highly anisotropic harmonic regime is shorten and the instability has quickly saturated.

We now move on with the concentration field global anisotropy, using the dimensionality parameter $\sin^2\gamma$, which reflects the directional anisotropy of a scalar field for statistically axisymmetric configurations [11,17,18]:

$$\sin^2\gamma = \frac{\int_0^\infty \int_0^\pi \mathcal{E}_{cc}(\boldsymbol{k},t)\sin^3\theta\, d\theta\, dk}{\int_0^\infty \int_0^\pi \mathcal{E}_{cc}(\boldsymbol{k},t)\sin\theta\, d\theta\, dk}, \tag{11}$$

where $\mathcal{E}_{cc}(\boldsymbol{k}) = \mathcal{E}_{cc}(k,\theta) = \hat{c}(-\boldsymbol{k})\hat{c}(\boldsymbol{k})/2$, so that $\iint k^2\mathcal{E}_{cc}(\boldsymbol{k},t)\sin\theta\, d\theta\, dk = \langle c^2\rangle/2$. Note that other anisotropic descriptors for scalar fields exist [19], and that for an isotropic state $\sin^2\gamma = 2/3$ unlike b_{33}.

The time evolution of $\sin^2\gamma$ is presented in Fig. 5(c) for runs F1A01, F1A1, and F2A01. For $F = 1$, the transition between the harmonic and subharmonic regimes is once again clearly visible. The conclusions regarding $\sin^2\gamma$ are similar to those of b_{33}. Anisotropy is maximal in the harmonic regime and increases ($\sin^2\gamma$ departs from 2/3): since the limit $\sin^2\gamma = 0$ corresponds to sheetlike structures, the information provided by $\sin^2\gamma$ is consistent with structures being more and more tilted while approaching the transition. Then global anisotropy decays ($\sin^2\gamma$ tends to 2/3) after the transition and during the subharmonic regime due to more intense turbulent transfers. The increase of $\sin^2\gamma$ is consistent with structures being dominantly vertically aligned. In the asymptotic state, $\sin^2\gamma$ roughly oscillates close to the isotropic value 2/3 and slightly departs from it as time goes by due to the domination of stratification over turbulence. The scenario is a bit different for $F = 2$: while vertical anisotropy b_{33} suddenly decreases, the concentration field is less anisotropic since

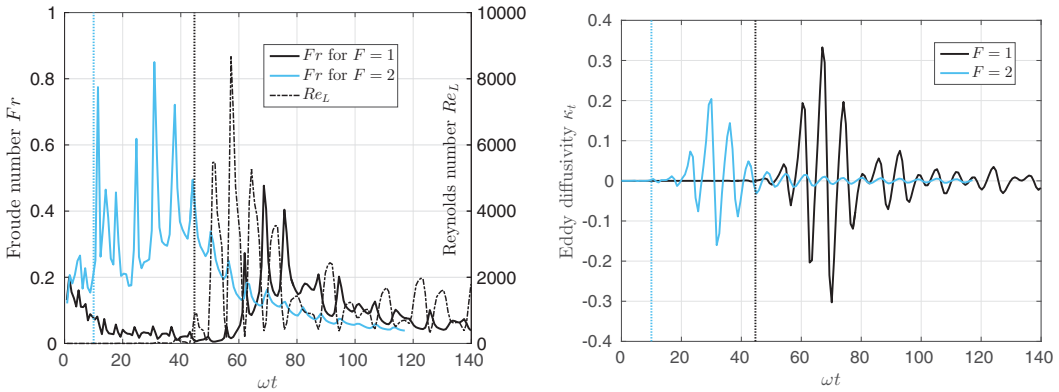

FIG. 6. Turbulent quantities for runs F1A01 (black) and F2A01 (light blue). (a) Froude number Fr; on the right y axis, Reynolds number Re_L for run F1A01. (b) Eddy diffusivity κ_t.

structures do not have time to be significantly tilted. In the asymptotic state, the concentration field is slightly more anisotropic with $F = 2$ than for $F = 1$: this is justified in the next section as well.

In this section, we have shown that the harmonic regime is highly anisotropic compared to the more turbulent subharmonic regime. Structures are dominantly vertically stretched and temporarily tilted toward the horizontal plane at the transition.

C. Turbulent quantities

In what follows, we pursue our analysis of one-point statistics to better characterize the transition between the harmonic and subharmonic regimes. In Sec. III A, it appeared that the growth of the mixing zone mainly occurs in the subharmonic regime, whereas in Sec. III B, global indicators revealed that the harmonic regime was more anisotropic than the subharmonic one. Hence, there is a severe change in the dynamics at the transition that we wish to better understand.

In the following, we investigate the Froude number $\mathrm{Fr} = \epsilon_{uu}/(NK_{uu})$, where $K_{uu} = \langle u_i u_i \rangle/2$ is the kinetic energy and ϵ_{uu} its dissipation rate, and the eddy diffusivity $\kappa_t = -L\langle u_3 c \rangle$. The time evolution of Fr is presented in Fig. 6(a) for runs F1A01 and F2A01. In the harmonic regime for $F = 1$, Fr is rather small because of the strong stratification. Then, from the transition and during the subharmonic regime, Fr significantly increases because turbulent exchanges become more intense, consistently with the strong growth of the mixing zone size $L(t)$ observed previously. Additional time evolutions of Fr are presented in the Appendix for larger and smaller F. Conjointly with the growth of Fr after the transition, the eddy diffusivity increases as well in Fig. 6(b). Note that κ_t changes sign due to the correlation $\langle u_3 c \rangle$, showing that turbulent exchanges develop and that part of the mixing is reversible. In the asymptotic state, both Fr and κ_t decrease with the decay of the turbulence intensity due to the saturation of the instability.

For $F = 2$, the harmonic regime is almost not visible, as pointed out previously for global anisotropy. The Froude number strongly increases towards larger values than for $F = 1$, as expected since production is more intense. The instability saturates more rapidly as well, the consequence being that b_{33} is asymptotically smaller for $F = 2$ than for $F = 1$. On the contrary, κ_t is weaker than for the case $F = 1$, very likely because the mixing occurs more rapidly. Hence, the concentration field is less turbulent for $F = 2$ than for $F = 1$, which is also in agreement with the scalar anisotropy $\sin^2\gamma$ being smaller for $F = 1$ than for $F = 2$.

The Reynolds number $\mathrm{Re}_L = K_{uu}^2/(\nu\epsilon_{uu})$, displayed in Fig. 6(a) for run F1A01, also shows the great enhancement of turbulence after the transition. From almost 0, it reaches its maximum value $\sim 9.10^3$ in the subharmonic regime and then settles around 10^3 in the asymptotic saturated state.

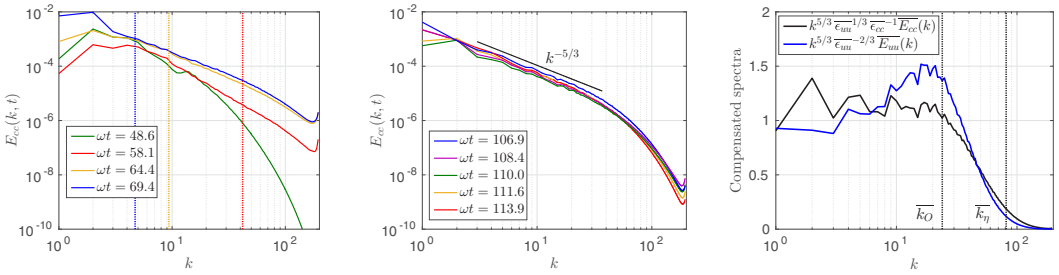

FIG. 7. Spherically averaged spectra for run F1A01. (a) E_{cc} at four different times during the subharmonic regime, corresponding to various extrema of $L(t)$; vertical dashed lines indicate the Ozmidov wave number k_O. (b) E_{cc} during one period in the asymptotic state. (c) Compensated spectra $\overline{E_{cc}}(k)$ and $\overline{E_{uu}}(k)$, along with the Ozmidov k_O and Kolmogorov k_η wave numbers; the period average is done for $\omega t \in [107; 114]$ corresponding to the spectra of panel (b).

The intensification of turbulent features and the creation of small scales participate as well to the reduction of global anisotropy from the transition, as mentioned in the previous section.

In this section, we have characterized the transition from the harmonic to subharmonic regime of the instability as a transition to turbulence. Indeed, the eddy diffusivity, the Froude number and the Reynolds number strongly increase at the transition, showing the enhancement of turbulent exchanges in the subharmonic regime.

D. Scale-by-scale analysis

In this section, we proceed with a scale-by-scale analysis of run F1A01 using the spherically averaged concentration variance and kinetic energy spectra

$$E_{uu}(k,t) = \frac{1}{2}\int_{S_k} \hat{u}_i(\boldsymbol{k})\hat{u}_i(-\boldsymbol{k})\, d^2\boldsymbol{k}, \quad E_{cc}(k,t) = \frac{1}{2}\int_{S_k} \hat{c}(\boldsymbol{k})\hat{c}(-\boldsymbol{k})\, d^2\boldsymbol{k}, \tag{12}$$

where $\hat{u}_i$ and $\hat{c}$ are the Fourier transforms of the fluctuating velocity and concentration fields, respectively, and S_k is the sphere of radius k. For the sake of brevity, results from other runs are not presented since scalings are quite similar.

We are interested only in time-averaged spectra $\overline{E_{cc}}$ and $\overline{E_{uu}}$ in the asymptotic state. Indeed, investigating the scalings of the kinetic energy and concentration variance spectra at various times during the growth of $L(t)$ makes no sense since the flow is highly unsteady: the intensity and slopes of E_{cc} and E_{uu} strongly vary. This is illustrated in Fig. 7(a), where E_{cc} is displayed at various times during the subharmonic regime, corresponding to different extrema of $L(t)$. At moderate ωt, all scales strongly change, whereas at later times, only the largest scales are modified. Note that the Ozmidov wave number $k_O = \sqrt{N^3/\epsilon_{uu}}$ significantly varies as well because of the sharp variations of $L(t)$.

The oscillations of E_{cc} are much smoother in the asymptotic state since the mixing is complete, as revealed in Fig. 7(b): only the largest scales are still slightly affected by the periodic forcing. Therefore, the spectra are period-averaged on the range $\omega t \in [107; 114]$ for further analysis. Averaging over six periods in the asymptotic state yields very similar results, with spectra slightly less intense, however, since the concentration variance decays over time.

The period-averaged spectra $\overline{E_{cc}}$ and $\overline{E_{uu}}$ are presented Fig. 7(c). The concentration spectrum exhibits a well-defined classical scaling $\overline{E_{cc}} \sim \overline{\epsilon_{cc}}\,\overline{\epsilon_{uu}}^{-1/3}k^{-5/3}$, with a plateau of order unity: this is expected since the concentration field experiences almost no more mixing mechanisms due to the instability, and consequently progressively returns to isotropy. On the contrary, there is no clear

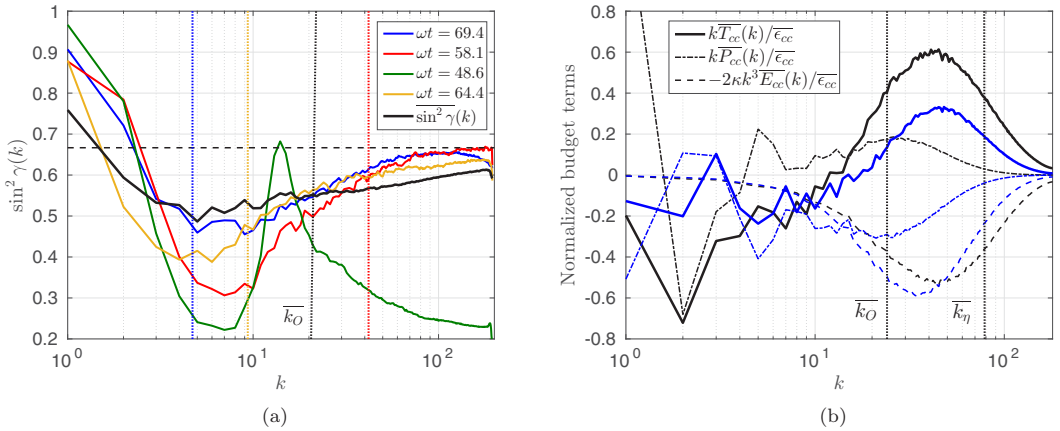

FIG. 8. (a) Spatial anisotropy of the concentration field $\sin^2\gamma(k)$ for run F1A01: period-averaged (black), and the same four times as Fig. 7(a). (b) Budget terms of the equations for $\overline{E_{cc}}$ (black) and $\overline{E_{uu}}$ (blue) for run F1A01: $-$ nonlinear transfers, $--$ dissipation, and $-\cdot$ production.

$k^{-5/3}$ scaling for $\overline{E_{uu}}$, or at least much narrower than for $\overline{E_{cc}}$, probably because of the forcing term; this might also be a consequence of the moderate Reynolds number.

Indeed, because of the moderate Reynolds number in the asymptotic state [$1000 \leqslant \overline{\mathrm{Re}_L} \leqslant 1500$; see Fig. 6(a)] large scales are still dominantly affected by the anisotropy due to stratification. This is well illustrated by the Ozmidov wave number, which is quite close to the Kolmogorov wave number $k_\eta = (\nu^3/\epsilon_{uu})^{1/4}$ in Fig. 7(c) . At larger Reynolds numbers, the return to isotropy would be more efficient, and thus k_O would go towards smaller wave numbers.

Now, we briefly address the scale-by-scale anisotropy of the concentration field using the spatial dimensionality parameter

$$\sin^2\gamma(k,t) = \frac{\int_0^\pi \mathcal{E}_{cc}(\boldsymbol{k},t)\sin^3\theta\, d\theta}{\int_0^\pi \mathcal{E}_{cc}(\boldsymbol{k},t)\sin\theta\, d\theta}, \tag{13}$$

shown in Fig. 8(a) for run F1A01. For the same reason as before, the period average in the asymptotic state is presented (in black), and $\overline{k_O}$ roughly separates anisotropic large scales from less anisotropic smaller ones. The spatial dimensionality parameter $\sin^2\gamma(k)$ is presented as well at the four same times of Fig. 7(a) and oscillates strongly at large scales. At the time where $L(t)$ is maximal ($\omega t = 69$), and thus where k_O is the smallest, there is a clear separation between anisotropic large scales and more isotropic small scales. On the other hand, at $\omega t = 48.6$, the Reynolds number is too small to distinguish large and small scales, with k_O out of the visible range.

Finally, we are interested in the budget terms of the equations for E_{uu} and E_{cc}, which read

$$\frac{\partial E_{xx}}{\partial t} + 2\nu k^2 E_{xx}(k,t) = T_{xx}(k,t) + P_{xx}(k,t), \tag{14}$$

where xx denotes either the velocity field uu or the concentration field cc, with $\nu = \kappa$. T_{xx} is the spherically averaged nonlinear transfer, and P_{xx} the production term, with, respectively, $P_{uu} = -2\mathcal{A}_t G_0[1 + F\cos(\omega t)]F_3$ and $P_{cc} = F_3/L$, with F_3 the spectrum of the mixed velocity-concentration correlation. The viscous, nonlinear, and production terms of these two equations are presented in Fig. 8(b), after averaging over the same period as in Fig. 7(c). The nonlinear transfers $\overline{T_{cc}}$ and $\overline{T_{uu}}$ are negative at large scales, and positive at smaller scales, showing that both kinetic energy and concentration variance are transferred from large to small scales. The dissipative term $-2\kappa k^2\overline{E_{cc}}$ balances quite well $\overline{T_{cc}}$ at small scales, whereas $2\nu k^2\overline{E_{uu}}$ is more intense than $\overline{T_{uu}}$: the latter feature probably explains why $\overline{E_{uu}}$ does not scale in $k^{-5/3}$. The production terms $\overline{P_{uu}}$ and

$\overline{P_{cc}}$ cover the entire range. Two noticeable features are that (1) for most wave numbers, $\overline{P_{cc}}(k) > 0$ whereas $\overline{P_{uu}}(k) < 0$, meaning that the main contribution of the flux F_3 is to extract kinetic energy and to convert it into concentration variance. And (2) the Ozmidov wave number quite well separates the large-scale region ($k < \overline{k_O}$) dominated by stratification where $\overline{P_{xx}} > \overline{T_{xx}}$, from the smaller scales dominated by the turbulence where $\overline{P_{xx}} < \overline{T_{xx}}$.

A difficulty of this turbulent instability is its unsteadiness. Consequently, spherically averaged spectra were presented only in the asymptotic state, where the Reynolds number has decreased due to the saturation of the instability: there is not a clear separation of scales between the Ozmidov and Kolmogorov wave numbers, indicating that large scales are more anisotropic and damped by stratification. Nevertheless, the concentration variance spectrum exhibits a $k^{-5/3}$ inertial range, and the kinetic energy and concentration variance are both transferred from large to small scales.

IV. THE IRREVERSIBLE MIXING

Now that the transition between the harmonic and subharmonic regimes has been characterized and interpreted as a transition to a turbulent state where the mixing zone grows significantly, we now wish to quantify the irreversible mixing of the flow using mixing efficiency and background potential energy.

A. Potential energies

To disentangle reversible exchanges from irreversible mixing, it is proposed to use the concepts of sorted density fields and background and available potential energies [9,10,20,21]. Recall that within the Boussinesq approximation, the density variations are linked to concentration through $\rho' \sim 2\mathcal{A}_t \rho_0 c$. The total potential energy being $E_p = \int \rho' g z \, dV$, we refer hereafter unambiguously to the normalized potential energy per unit surface as

$$e_p(t) = \frac{E_p(t)}{4\pi^2 \rho_0} = 2\mathcal{A}_t G_0 \int_{L_\eta/2}^{2\pi - L_\eta/2} \langle C \rangle_H(z,t) z \, dz, \tag{15}$$

where the penalized volume of the simulations characterized by L_η has been discarded. Since e_p can be modified by adiabatic processes, i.e., reversible mixing, we are interested in the sorted concentration field $C(z^*)$, which depends only on the probability density function (p.d.f.) of the concentration field $f(C)$. z^* is the position in the state of minimum potential energy attainable through an adiabatic redistribution of C. This minimum potential energy, called the background potential energy, is defined as

$$e_p^b(t) = 2\mathcal{A}_t G_0 \int_{z_{\min}}^{z_{\max}} C(z^*) z^* \, dz^* \tag{16}$$

and reflects the amount of gravitational potential energy e_p expanded in mixing the two fluids. The reference state is computed from the p.d.f. as in Ref. [20] according to

$$z^*(C) = z_{\min} + (z_{\max} - z_{\min}) \int_0^C f(C') dC', \tag{17}$$

where $z_{\min}$ and $z_{\max}$ are the boundaries of the fluid domain in which the p.d.f. is built, and C' a dummy variable. Here $z_{\min} = L_\eta/2$ and $z_{\max} = 2\pi - L_\eta/2$, and $f(C)$ is built with 4096 points [we have checked that more points for the p.d.f. do not modify $z^*(C)$]. Then, the available potential energy $e_p^a = e_p - e_p^b$ corresponds to the energy that would be released during an adiabatic transformation toward the background state. In other words, e_p^a is the fraction of total potential energy which can be converted into e_p^b through irreversible mixing.

We are now interested in the energy contents of run F1A01. The p.d.f. of the concentration field is presented in the inset of Fig. 9(a) at three different times. Initially, $f(C)$ is sharply peaked around

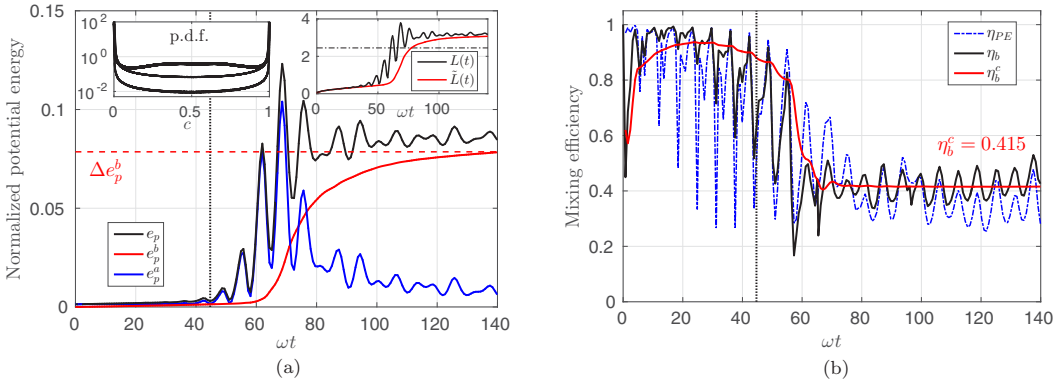

FIG. 9. Potential energy and mixing efficiency for run F1A01. (a) Total, background, and available potential energies e_p, e_p^b, and e_p^a. First inset: p.d.f. at increasing time: $t = 0$, $\omega t = 40$, and $\omega t \simeq 69$ when $L(t)$ is maximal. Second inset: unsorted $L(t)$, sorted $\tilde{L}(t)$. (b) Instantaneous mixing efficiencies η_{PE} (blue) and η_b (black), along with the cumulative mixing efficiency η_b^c (red).

$C = 0$ and $C = 1$. At $\omega t = 69$ when $L(t)$ is maximum, there is a noteworthy bump around $C = 0.5$ reflecting that there is more and more mixing.

The time evolution of the three potential energies is displayed in Fig. 9(a): the background potential energy (red) increases monotonically as the irreversible mixing of the two fluids progresses, which also results in a decrease of the available potential energy (blue). Notably, e_p^b increases substantially only after the transition, and this is verified for all runs. The gain of background potential energy over the whole simulation can be evaluated as follows, assuming a profile in three parts for $C(z^*)$ (constant, linear, and constant):

$$\Delta e_p^b = \frac{\mathcal{A}_t G_0}{12}\left(\tilde{L}_{\text{end}}^2 - L_0^2\right). \tag{18}$$

In the previous formula, $\tilde{L}_{\text{end}}$ is the final mixing zone size computed with the sorted profile $C(z^*)$, close to but slightly smaller than L_{end}. For run F1A01, $\Delta e_p^b = 0.079$, which is in good agreement with the plot of Fig. 9(a). The gain in background potential energy for the other runs is indicated in Table I. One may remark that Δe_p^b can vary by more than one order of magnitude (see runs F07A045 and F055A015) and is thus quite sensitive to the choice of parameters: in particular, for two simulations with similar L_{sat}, Δe_p^b may differ since it depends linearly on $\mathcal{A}_t$.

An additional essential outcome of this section is the following one. The available potential energy e_p^a is maximal in Fig. 9(a) when $L(t)$ reaches the saturation prediction L_{sat} at $\omega t \simeq 70$. This explains why in Ref. [7] and in Fig. 3(a) the final size L_{end} always exceeds the prediction. Indeed, L_{sat} corresponds only to the *saturation* of the instability. After the saturation, the available potential energy is released in the flow, either as kinetic or background potential energy. This additional background potential energy pursues the irreversible mixing and L increases towards values slightly larger than L_{sat}.

B. Mixing efficiencies

In this section, we wish to estimate the mixing efficiency of our turbulent flows, if any sense can be given to an instantaneous mixing efficiency in a framework with a periodic forcing. We consider three different possibilities to compute the mixing efficiency hereafter.

A first definition is borrowed from Ref. [22], where the mixing efficiency reads

$$\eta_{PE} = \frac{\epsilon_{PE}}{\epsilon_{PE} + \epsilon_{uu}}, \quad \epsilon_{PE} = N^2 \epsilon_{cc} \left(\frac{d\langle C\rangle_H}{dz}\right)^{-2} \tag{19}$$

and is like a flux Richardson number, with ϵ_{PE} the dissipation of potential energy. According to the authors of the latter reference, this definition is more robust than others which rely on the scalar flux $\langle u_3 c \rangle$. Indeed, $\langle u_3 c \rangle$ accounts for reversible mixing. Nevertheless, this definition intrinsically takes into account both reversible and irreversible mixing since it is not based on $C(z^*)$. The instantaneous mixing efficiency η_{PE} is given in Fig. 9(b) for run F1A01: the oscillations are quite wide because ϵ_{uu} and ϵ_{cc} oscillate in phase opposition. After the transition, η_{PE} decays due to the strengthening of the turbulence, i.e., the increase of ϵ_{uu}. In the saturated state, η_{PE} roughly settles around 0.35, which is a common value for mixing efficiency in stratified turbulent flows [22].

The second definition can be found in Refs. [10,21,23] and is based on the background potential energy, so that it should be more relevant in terms of quantifying the irreversible mixing. The instantaneous mixing efficiency reads

$$\eta_b = \frac{\epsilon_b}{\epsilon_b + \epsilon_{uu}}, \quad \epsilon_b = \frac{1}{V}\frac{dE_p^b}{dt} \tag{20}$$

where ϵ_b is the dissipation rate of the background potential energy density, with V the volume of the fluid domain. The time evolution of η_b in Fig. 9(b) is quite similar to the one of η_{PE}, but with oscillations of smaller amplitudes: this is expected since reversible mixing is excluded while using ϵ_b rather than ϵ_{cc}. Note that in the asymptotic state, in average $\eta_b \simeq 0.42 > \eta_{PE}$.

However, although necessary to capture the different regimes of the instability, it becomes clear that there is no real meaning to an instantaneous mixing efficiency in a periodically forced system. Instead, we compute the cumulative mixing efficiency [10]

$$\eta_b^c(t) = \frac{\int_0^t \epsilon_b(t')\,dt'}{\int_0^t \epsilon_b(t')\,dt' + \int_0^t \epsilon_{uu}(t')\,dt'}. \tag{21}$$

This definition gives a smooth time evolution compared to the previous instantaneous mixing efficiencies η_{PE} and η_b. The final value for run F1A01 is $\eta_b^c = 0.415$, which is close to the final value of the instantaneous mixing efficiency η_b. Final values of η_b^c for the other runs are gathered in Table I as well: it is worth noting that η_b^c is much less sensitive to the control parameters than Δe_p^b. A remarkable result is that the cumulative mixing efficiency tends to decrease with larger F, irrespective of L_{sat}. This is expected since with larger F, the instability saturates rapidly, and thus there is less time for mixing.

C. Conclusions regarding mixing

The particularities here are that the flow is unsteady because of the periodic forcing, and that most of the mixing happens in the subharmonic regime, which represents a short time of the simulation, and in a small domain between the two reservoirs of pure fluids. Nevertheless, using the concept of sorted density field, we have been able to compute the background potential energy of our flow. This is a completely unique feature compared to the paper at the origin of the theory [7]. Four important findings should be stressed:

(1) Irreversible mixing starts only with the growth of the mixing zone after the transition.

(2) The gain in background potential energy Δe_p^b strongly depends on the control parameters of the instability: hence, configurations with similar L_{sat} can have different Δe_p^b.

(3) At saturation, available potential energy e_p^a is maximal and partially released as background potential energy, which causes the mixing zone to increase beyond L_{sat}.

(4) The final cumulative mixing efficiency η_b^c decreases with larger forcing parameters F because the instability, and thus mixing, is shortened.

Although there is a conceptual complexity of evaluating mixing efficiency in a transitory and periodically forced system, the different estimations tend to qualify the Faraday instability as an efficient mixing process.

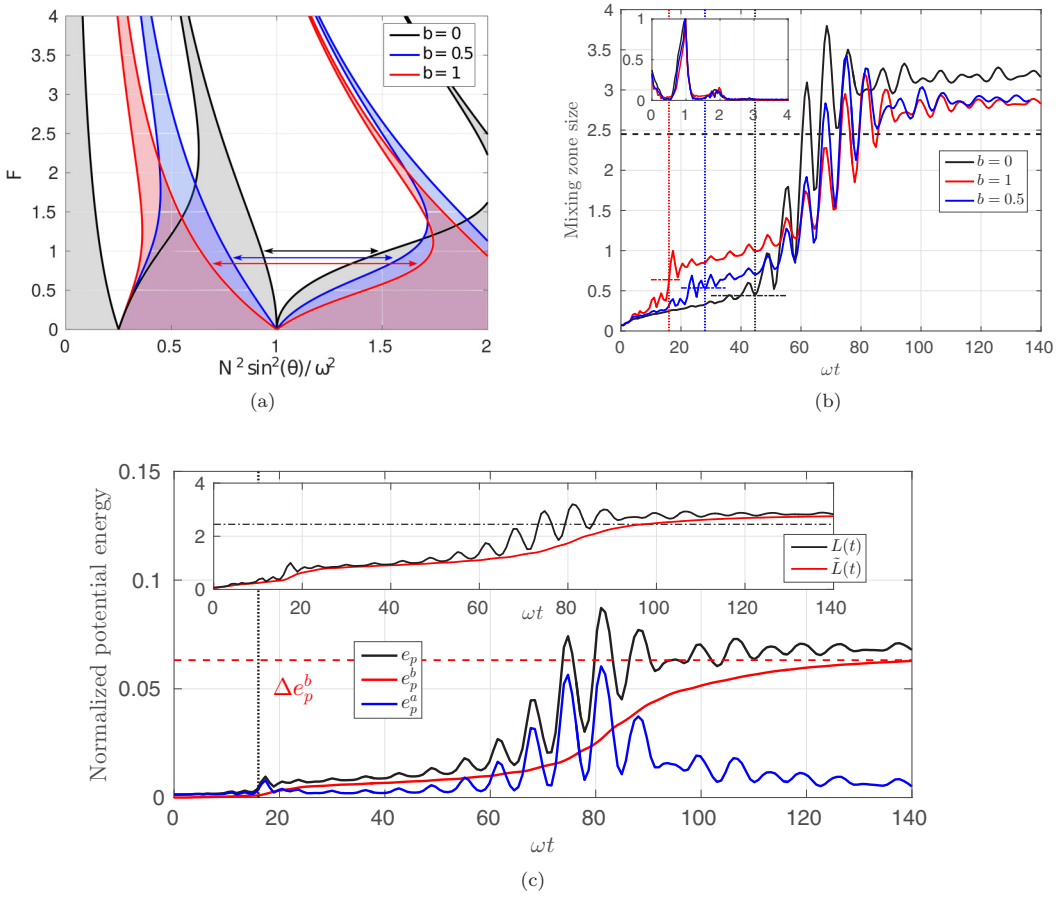

FIG. 10. (a) Stability diagram for the multiple-frequency case: $b = 0$ (black), $b = 0.5$ (run F1A01b05, blue), and $b = 1$ (run F1A01b1, red). Arrows indicate the new extent of the first harmonic tongue. (b) $L(t)$ for runs F1A01b05 and F1A01b1. (c) e_p, e_p^b, and e_p^a for run F1A01b1. Inset: sorted $\tilde{L}$ and unsorted L mixing zone sizes.

V. MULTIPLE-FREQUENCY FORCING

Is it possible, given a set of control parameters $(\mathcal{A}_t, F, \omega)$, to shorten the duration of the harmonic regime? It is proposed to answer this question here, which is motivated by the following reason: it has been shown in Sec. IV that no mixing occurs during the harmonic regime. Then, by reducing the harmonic regime one should get the final size of the mixing zone more rapidly. There are two obvious possibilities to shorten the harmonic regime: (1) According to Fig. 3(a), one can increase F. (2) By choosing wisely $\mathcal{A}_t$, ω, and L_0, the initial condition $2\mathcal{A}_t G_0/(L_0\omega^2)$ could be only in the first subharmonic tongue of Fig. 1.

However, from a practical point of view, the control parameters are related through $A_m = FG_0/\omega^2$, where A_m is the amplitude of the vertical periodic forcing [24]. Let us further assume that one cannot exceed $F = 1$ for some reasons: $\mathcal{A}_t$ and L_0 being imposed by the nature of the fluids, the initial condition could fall beyond the first subharmonic tongue.

In such a case under the constraint $F \leqslant 1$, we propose to use a multiple-frequency forcing. This idea is not new and was notably used in Ref. [3] for immiscible fluids to study pattern formation at the interface. Here the modulated gravity $G_0[1 + F\cos(\omega t)]$ is basically replaced by $G_0[1 + F\cos(\omega t) - bF\cos(2\omega t)]$, where $b \leqslant 1$ is the multiple-frequency parameter. The idea is

that the subharmonic regime of $\cos(2\omega t)$ may affect the harmonic regime of $\cos(\omega t)$. In terms of stability, the classical Mathieu diagram of Fig. 1 is modified as in Fig. 10(a), where two noticeable features should be pointed out: (1) the first harmonic tongue is made quite larger for moderate forcing parameters $F \simeq 1$: this is not *a priori* what we want; and (2) the marginal stability curve is not modified, so that the saturation prediction (1) remains valid for this kind of multiple-frequency forcing.

Two cases are investigated in Fig. 10(b) for both $b = 0.5$ (run F1A01b05) and $b = 1$ (run F1A01b1). It appears that the harmonic regime is more than twice as short ($b = 1$) as the case without multiple frequency ($b = 0$): this is not intuitive given the extension of the harmonic tongue in Fib. 10(a). In fact, the multiple-frequency forcing acts as an initial booster for the growth of the mixing zone, so that N^2/ω^2 leaves rapidly the harmonic tongue. After this initial sudden growth, $L(t)$ evolves smoothly, before increasing significantly a second time. The maximum of $L(t)$ is thus reached later after the transition compared to the case $b = 0$.

Moreover, it is worth noting that for both $b = 0.5$ and $b = 1$ in Fig. 10(b), the final size of the mixing zone L_{end} is closer to the prediction than for $b = 0$. This is because when $L > L_{\text{sat}}$, the available potential energy e_p^a is smaller with $b \neq 0$ than with $b = 0$, as revealed in Fig. 10(c) for $b = 1$, consistently with the argument proposed in Sec. IV. Note that despite the multiple frequency, e_p^b still increases only after the transition. The final cumulative mixing efficiency η_b^c for $b = 0.5$ and $b = 1$ is similar to the one with $b = 0$, as summarized in Table I.

In conclusion, we have proposed a way to reduce the duration of the harmonic regime under a constraint of control parameters. This simple multiple-frequency forcing enhances the turbulent mechanisms linked to the transition and yields a final size of the mixing zone L_{end} closer to the prediction L_{sat}. Note that more complex forcing terms could be analyzed, for instance, with an additional phase shift $\cos(\omega t) - b\cos(2\omega t + \phi_b)$, or with a combination of sine and cosine, but this is out of the scope of this study. The advantage of this simple multiple-frequency forcing is that it preserves the saturation prediction (1).

VI. CONCLUSIONS

When a stable stratification of two miscible fluids is vertically and periodically excited, a turbulent mixing zone can grow in size as a result of the Faraday instability, depending on the control parameters. It reaches a final state when parametric resonances terminate: the final saturated size L_{sat} was predicted in Ref. [7] and assessed for a wide range of parameters, mainly with DNSs of 256^3 and 512^3 points. In the latter reference, a transition of the instability from a harmonic to a subharmonic regime was observed for simulations in a homogeneous framework.

In the present work, we have observed numerically for the first time the transition of the miscible Faraday instability from a harmonic to a subharmonic regime in the full inhomogeneous system accounting for the two reservoirs of pure fluids. To this end, multiple DNSs with 1024^3 points were performed using a pseudospectral code. To ensure the periodicity of the concentration field in the vertical inhomogeneous direction, a penalization method was implemented. The unique features of this study, with respect to Ref. [7], are the analysis of turbulent one-point and two-point statistics in the full inhomogeneous system, along with the investigation of irreversible mixing through mixing efficiencies and background potential energy, and multiple-frequency forcing. The main findings are summarized below.

First, we identified a robust scenario describing the dynamics of structures before and after the transition. In the harmonic regime, the velocity and concentration fields are highly anisotropic because vertically elongated structures develop. A sudden decrease in anisotropy occurs at the transition since structures are temporarily tilted horizontally, and turbulence is strongly enhanced, which creates small scales that partially restore isotropy. Then, in the subharmonic regime, global anisotropy slightly increases because structures align again in the vertical direction. In the saturated state, global anisotropy roughly oscillates around a constant value. For larger forcing parameters, the harmonic regime is shorter so that the global anisotropy immediately decreases. Regarding the

mixing zone size $L(t)$, it strongly increases only from the transition. For similar final states L_{end}, various transients can be observed depending on the control parameters.

One-point turbulent quantities such as the Froude number, the Reynolds number, and the eddy diffusivity clearly confirm that the harmonic to subharmonic transition is a sharp transition to turbulence. In the asymptotic regime, after the saturation of the instability, the Reynolds number remains moderate: as a consequence, the Ozmidov wave number is close to the Kolmogorov one, meaning that most scales of the flow are damped by stratification. Nevertheless, the time-averaged concentration variance spectrum $\overline{E_{cc}}$ exhibits a $k^{-5/3}$ range, and kinetic energy and concentration variance are transferred from large to small scales.

Afterwards, using the probability density function of the concentration field, we have computed the time evolution of the background potential energy e_p^b. This is a measure of the irreversible mixing of the flow, which starts only after the transition. The gain of background potential energy Δe_p^b between the initial and final states strongly depends on control parameters, so that two configurations with the same L_{sat} can give different Δe_p^b. A major outcome of this analysis is that at saturation of the instability, available potential energy e_p^a is partially released as background potential energy e_p^b in the flow: this additional irreversible mixing causes L to grow beyond L_{sat}. This notably explains why in Ref. [7] the final size obtained numerically L_{end} always exceeds the prediction L_{sat}.

Then three different definitions of the mixing efficiency were compared: we argue that it might not be relevant to investigate instantaneous mixing efficiencies since our flow is highly unsteady and mixing occurs within a limited time and space domain. The cumulative mixing efficiency η_b^c, however, has a smooth evolution. It is worth noting that its final value decreases with larger forcing parameters F, irrespective of L_{sat}: indeed, with larger F, the instability saturates quickly and the mixing process is shortened.

Finally, it was shown that under some constraints of the control parameters, the harmonic regime can be shrunk by using a multiple-frequency forcing, with pulsations ω and 2ω. Our particular choice preserves the saturation criterion.

In conclusion, the harmonic regime is highly anisotropic and almost no mixing occurs. Its duration can be reduced with the use of multiple-frequency forcing. At the transition, the turbulence is triggered, and irreversible mixing is greatly enhanced. In the subharmonic regime, the mixing zone grows significantly. At saturation of the instability, the final size exceeds the prediction because available potential energy is released as background potential energy in the flow, which produces more mixing.

ACKNOWLEDGMENTS

DNSs were performed at the French computing center CEA. L.G. was partially funded by the Agence Nationale de la Recherche, ANR-13-JS09-0004-01 (STRATIMIX).

APPENDIX: INFLUENCE OF THE FORCING PARAMETER

In this Appendix, we are interested in the impact of the forcing parameter F on the triggering of the instability and turbulent intensity.

In Fig. 3(a), it was shown that with $F = 2$ the instability was triggered much before the cases with $F = 1$. Afterwards, it was revealed that the turbulence was more intense with $F = 2$ than with $F = 1$ with the Froude number in Fig. 6(a). These two features are recovered from $F = 0.7$ to $F = 8$ in Figs. 11(a) and 11(b), using the results of the DNSs gathered in Table I.

First, when the forcing parameter F is increased, the growth of Fr happens earlier and is more intense. Namely, for $F = 5.46$ and $F = 8$, the turbulence is three to four times more intense than for $F = 1$: accordingly, the harmonic regime does not exist. The conclusions are similar in Fig. 11(b)

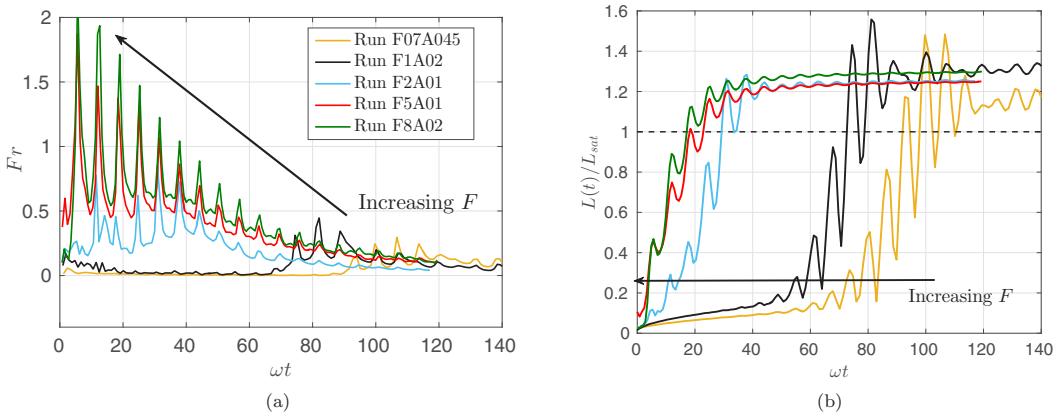

FIG. 11. Time evolutions for increasing F, corresponding to the DNS runs of Table I. (a) Fr; (b) $L(t)/L_{\rm sat}$.

for the mixing zone size $L(t)$: the larger F, the shorter the harmonic regime. Note that at larger F, the initial growth of $L(t)$ is always very sharp and hardly depends on $k_{\rm peak}$, unlike at small F in Fig. 4 for $F = 1$.

[1] M. Faraday, XVII. On a peculiar class of acoustical figures; and on certain forms assumed by groups of particles upon vibrating elastic surfaces, Philos. Trans. R. Soc. London **121**, 299 (1831).

[2] S. Douady, Experimental study of the Faraday instability, J. Fluid Mech. **221**, 383 (1990).

[3] W. S. Edwards and S. Fauve, Patterns and quasi-patterns in the Faraday experiment, J. Fluid Mech. **278**, 123 (1994).

[4] F. Zoueshtiagh, S. Amiroudine, and R. Narazanan, Experimental and numerical study of miscible Faraday instability, J. Fluid Mech. **628**, 43 (2009).

[5] S. Amiroudine, F. Zoueshtiagh, and R. Narayanan, Mixing generated by Faraday instability between miscible liquids, Phys. Rev. E **85**, 016326 (2012).

[6] D. Benielli and J. Sommeria, Excitation and breaking of internal gravity waves by parametric instability, J. Fluid Mech. **374**, 117 (1998).

[7] B.-J. Gréa and A. Ebo Adou, What is the final size of turbulent mixing zones driven by the Faraday instability, J. Fluid Mech. **837**, 293 (2018).

[8] S. V. Diwakar, F. Zoueshtiagh, S. Amiroudine, and R. Narayanan, The Faraday instability in miscible fluid systems, Phys. Fluids **27**, 084111 (2015).

[9] K. Winters, P. N. Lombard, J. J. Riley, and A. D'Asaro, Available potential energy and mixing in density-stratified fluids, J. Fluid Mech. **289**, 115 (1995).

[10] W. R. Peltier and C. P. Caufield, Mixing efficiency in stratified shear flows, Annu. Rev. Fluid Mech. **35**, 135 (2003).

[11] B.-J. Gréa, The rapid acceleration model and the growth rate of a turbulent mixing zone induced by Rayleigh-Taylor instability, Phys. Fluids **25**, 015118 (2013).

[12] T. B. Benjamin and F. Ursell, The stability of the plane free surface of a liquid in vertical periodic motion, Proc. R. Soc. London A **225**, 505 (1954).

[13] K. Kumar and L. Tuckerman, Parametric instability of the interface between two fluids, J. Fluid Mech. **279**, 49 (1994).

[14] A. Ebo Adou and L. S. Tuckerman, Faraday instability on a sphere: Floquet analysis, J. Fluid Mech. **805**, 591 (2016).

[15] C. Jause-Labert, F. S. Godeferd, and B. Favier, Numerical validation of the volume penalization method in three-dimensional spectral simulations, Comput. Fluids **67**, 41 (2012).

[16] See Supplemental Material at http://link.aps.org/supplemental/10.1103/PhysRevFluids.4.044502 for 3D videos of the following runs: (1) run F1A02 for the quantity ρ'/ρ_0; at $F = 1$, the transition happens sooner than with $\mathcal{A}_t = 0.1$. (2) Run F2A01 for the quantity ρ'/ρ_0; at $F = 2$, there is no visible harmonic regime. (3) Run F1A1 for the quantity ρ'/ρ_0; this is the case with the largest Atwood number, $\mathcal{A}_t = 0.1$, and the transition is delayed compared to $\mathcal{A}_t = 0.02$. (4) Run F1A02k5 for the quantity ρ'/ρ_0; energy is injected at larger scales than in run F1A02, and the harmonic regime is shorter.

[17] C. Cambon and B.-J. Gréa, The role of directionality on the structure and dynamics of strongly anisotropic turbulent flows, J. Turbulence **14**, 50 (2013).

[18] A. Burlot, B.-J. Gréa, F. S. Godeferd, C. Cambon, and O. Soulard, Large Reynolds number self-similar states of unstably stratified homogeneous turbulence, Phys. Fluids **27**, 065114 (2015).

[19] A. Briard, T. Gomez, and C. Cambon, Spectral modeling for passive scalar dynamics in homogeneous anisotropic turbulence, J. Fluid Mech. **799**, 159 (2016).

[20] M. S. Davies Wykes and S. B. Dalziel, Efficient mixing in stratified flows: Experimental study of a Rayleigh-Taylor unstable interface within an otherwise stable stratification, J. Fluid Mech. **756**, 1027 (2014).

[21] M. S. Davies Wykes, G. O. Hughes, and S. B. Dalziel, On the meaning of mixing efficiency for buoyancy-driven mixing in stratified turbulent flows, J. Fluid Mech. **781**, 261 (2015).

[22] S. K. Venayagamoorthy and J. R. Koseff, On the flux Richardson number in stably stratified turbulence, J. Fluid Mech. **798**, R1 (2016).

[23] A. Venaille, L. Gostiaux, and J. Sommeria, A statistical mechanics approach to mixing in stratified fluids, J. Fluid Mech. **810**, 554 (2017).

[24] Y. A. Gaponenko, M. Torregrosa, V. Yasnou, A. Mialdun, and V. Shevtsova, Dynamics of the interface between miscible liquids subjected to horizontal vibration, J. Fluid Mech. **784**, 342 (2015).